Accepted Manuscript

Petroleum Geoscience

3D-seismic interpretation and fault slip potential analysis from hydraulic fracturing in the Bowland Shale, UK

Sirawitch Nantanoi, Germán Rodríguez-Pradilla & James Verdon

DOI: https://doi.org/10.1144/petgeo2021-057

To access the most recent version of this article, please click the DOI URL in the line above. When citing this article please include the above DOI.

Received 20 July 2021
Revised 22 October 2021
Accepted 1 November 2021

3D-seismic interpretation and fault slip potential analysis from hydraulic fracturing in the Bowland Shale, UK

Manuscript in preparation for the journal Petroleum Geoscience

First version submitted in July 2021

Second version submitted in October 2021

Authors:

Sirawitch Nantanoi, Germán Rodríguez-Pradilla, and James Verdon

School of Earth Sciences, University of Bristol, Bristol, United Kingdom

Corresponding authors:

SN: s.nantanoi@bristol.ac.uk; https://orcid.org/0000-0002-6949-8594

GRP: dd20141@bristol.ac.uk; https://orcid.org/0000-0001-8917-9243

JV: james.verdon@bristol.ac.uk; https://orcid.org/0000-0002-8410-2703

Abstract

The Bowland Shale Formation is one of the most promising targets for unconventional exploration in the United Kingdom, with estimated resources large enough to supply the country's entire natural gas consumption for 50 years. However, development of the Bowland Shale has stalled due to concerns over hydraulic-fracturing induced seismicity. Only three wells have been drilled and hydraulic fractured to date in the Bowland Shale, and all three wells have produced levels of seismicity of sufficient magnitude to be felt at the surface. Susceptibility to induced seismicity will be determined by the presence of critically-stressed faults. However, such faults can go undetected in conventional interpretation of 2D or 3D seismic surveys if they are shorter that the resolution retrievable from a seismic survey, or if they have low (and in some cases even zero) vertical displacement. In such cases, the faults that cause induced seismicity may only be visible via microseismic observations once they are reactivated. To better identify fault planes from 3D seismic images, and their reactivation potential due to hydraulic fracturing, a high-resolution fault-detection attribute was tested in a 3D seismic survey that was acquired over the Preston New Road site, where two shale-gas wells were hydraulic-fractured in the Bowland Shale in 2018 and 2019, obtaining fault planes with lengths between 400 and 1500 meters. Fault slip potential was then estimated by integrating the obtained faults with the formation's stress and pore pressure conditions (with the Bowland shale also being significantly overpressured), and several critically stressed faults were identified near the previously hydraulic fractured wells. However, the faults that induced the largest seismic events in the Preston New Road site, of approximately 200 meters in length for seismic

events of magnitudes below 3.0 (as imaged with a multicomponent, downhole microseismic monitoring array deployed during the hydraulic fracturing stimulations), could not be identified in the 3D seismic survey that only mapped fault planes larger than 400 meters in length.

Introduction

The Bowland Shale Formation is one of the most promising targets for unconventional exploration in the UK because of its high Total Organic Content (TOC) (typically 1-3%, but can reach up to 8%), porosity (4-7%), and brittleness (>30% of silica content) (Andrews, 2013; Smith et al., 2010). Located at depths from 2,000 to 4,750 m, stretching across central Great Britain (Figure 1a), the Bowland Shale is composed of dark grey shale with interbedded limestone, siltstone, calcareous mudstone, and sandstone (Andrews, 2013). The study area is located in the NW England's Bowland Basin, which started to develop during the Late Devonian to Carboniferous by the rifting in the N-S to NW-SE direction (Anderson & Underhill, 2020). After that, this area was influenced by various geological processes including the post-rift thermal subsidence in the Pennsylvanian and the Variscan Orogeny in the Early Permian, leaving the area heavily deformed (Anderson & Underhill, 2020). The stratigraphic column of the Bowland Basin is shown in Figure 2, where the Bowland Shale was depicted sitting on top of the Worston Shale Group, and below the Millstone Grit Group. The Bowland Shale been estimated by the British Geological Survey (BGS) to potentially host P90, P50, and P10 resources of 822, 1,329, and 2,281 trillion cubic feet (tcf) (23.3, 37.6, and 64.6 trillion cubic meters (tcm)) of natural gas respectively (Andrews, 2013). A 10% recovery rate of the P50 value translates to almost 50 years of UK gas consumption (Andrews, 2013).

Despite the potential size of this resource, development of the Bowland Shale has stalled due to concerns over hydraulic-fracturing induced seismicity (HF-IS). The UK's Department of Energy and Climate Change (DECC) first imposed a moratorium in 2011 in response to a magnitude M_L 2.3 earthquake at the Preese Hall well (Figure 1c) (Clarke et al., 2014). This moratorium was later lifted by DECC in December 2012 (OGA, 2019), with the implementation of a strict Traffic Light Scheme (TLS) with a red light threshold set at M_L 0.5 to suspend injection (Kendall et al., 2019). However, further hydraulic fracturing at the Preston New Road wellsite (figure 1c) produced an M_L 1.5 earthquake in 2018 (Clarke et al., 2019a), and an M_L 2.9 earthquake in 2019 (Kettlety et al., 2021). The fault planes which are believed to cause both M_L 1.5 and M_L 2.9 induced seismicity at the PNR site were identified by mapping the seismic event ($M_L > 0$) locations during an injection hiatus (Clarke et al., 2019a) and utilizing the locations of the aftershock events to delineate the fault plane (Kettlety et al., 2021). Also, the focal mechanisms of the largest induced earthquakes exhibit a strike-slip mechanism with nearly vertical nodal planes, making these fault planes difficult to detect in reflection seismic datasets as no strike-slip faults typically have small (and in some cases null) vertical offsets. In response to these anomalously large seismic events, some of which were also felt by local communities, the UK government has imposed a further indefinite moratorium on shale gas development. Hence, there is a clear need to better manage the risks posed by induced seismicity if further development of this resource is to take place.

Induced seismicity takes place when subsurface activities, such as hydraulic fracturing, create perturbations in the pore pressure and/or stress field in the surrounding rocks. If a pre-existing fault is present that is near to its critical stress state, then these perturbations may be sufficient to trigger

slip, resulting in induced seismicity. The magnitude of induced earthquakes will be determined by the dimensions of the resulting slip; as such, induced seismic magnitudes may be influenced by the scale of the perturbation (e.g., Shapiro et al., 2011), by the size of faults present in the vicinity of the stimulated well, or by the smoothness (or planarity) of the fault planes, as smoother ("simpler") faults produce bigger earthquakes (Wesnousky, 1988). For HF-IS to occur, several necessary conditions must therefore be met: a fault of sufficient size must be present in the subsurface in the vicinity of the stimulated well, the in-situ stress conditions must be such that the fault is close to its critical point, and the perturbation created by the stimulation must be of sufficient size to move the conditions on the fault to failure.

In a broad sense, there are two methods by which the risks of HF-IS could be mitigated: real-time modification of injection schemes, and pre-operation site selection based on mapping of subsurface faults. Real-time HF-IS mitigation involves decision-making based on observed microseismicity during operations. Perhaps the simplest form of real-time HF-IS decision-making are TLSs, where injection rates are reduced or stopped depending on the magnitudes of induced events (e.g., Verdon and Bommer, 2021). Alternatively, statistical forecasting of expected magnitudes can also be used to guide decision-making during stimulation (e.g., Verdon and Budge, 2018; Clarke et al., 2019a; Kwiatek et al., 2019; Kettlety et al., 2021).

As described above, for HF-IS to occur, a pre-existing fault that is critically stressed must be present in the vicinity of the well. Hence, if we were able to obtain a complete understanding of the position and orientation of faults in the subsurface, then HF-IS could, in theory, be mitigated by avoiding sites where critically-stressed faults are present (i.e. faults that are optimally oriented relative to the maximum principal stress, to have the maximum shear stress acting upon them, which could make these faults to slip if the shear stress exceeds the faults' friction; discussed in more detail in the Fault Slip Potential section and in Figure 11). It is this possibility that we investigate in this study, with a focus on the HF-IS observed at the Preston New Road (PNR) site in 2018 – 2019 (Clarke et al., 2019a; Kettlety et al., 2021). This site offers several high quality, publicly-available datasets, including high-resolution microseismic data acquired during stimulation, 3D reflection seismic data, and geophysical well logs.

This study aims to compare the fault planes identified using microseismic observations (i.e., location of microseismic events, and focal planes of higher-magnitude events) as those responsible for the PNR HF-IS (Figure 3), with structures identified in interpretation of 3D seismic data acquired at the site. Our interpretation of the 3D seismic begins with well-to-seismic calibration, followed by manual horizon and fault picking. We follow this with the application of seismic attributes, including similarity, spectral decomposition, curvature, and an automated fault detection attribute. While these methods identify numerous faults around the PNR site, they struggle to identify the faults responsible for the HF-IS, highlighting the challenges of basing HF-IS mitigation on pre-operational site selection.

Preston New Road Site Description and Datasets

The Bowland Shale was deposited in a marine environment with relative sea level fluctuations, causing alternating changes in lithology between deltaic and deep marine facies (Andrews, 2013). Its mineral content consists of 56-59% clay, 45% quartz, and 10% carbonate (Smith, et al., 2010). It was deposited in a very tectonically active environment: starting from the formation of the Bowland Basin during the Devonian and Carboniferous periods, thermal subsidence during the Pennsylvanian (Namurian and Westphalian stages), and exhumation from the Variscan Orogeny in the late Carboniferous and Permian periods (see stratigraphic column in Figure 2) (Anderson & Underhill, 2020). This tectonic complexity can be seen in 3D seismic data.

To date, activities in the Bowland Shale have been focused on the Fylde Peninsula, Lancashire, where stimulation has taken place at the Preese Hall and PNR sites near Blackpool (Figure 1b). This area is covered by a 3D reflection seismic dataset, pre-stack depth migrated, of around 10 by 10 km (Figure 1c). The dataset was acquired in 2012 after the first felt seismic events associated with hydraulic fracturing were reported in 2011 at the Preese Hall 1 well (Clarke et al., 2014). One fault near the Preese Hall 1 well was observed in this 3D seismic dataset, with very similar location and orientation as one nodal plane of one of the largest-magnitude events of M_L 2.3 registered during the well's hydraulic stimulation (Clarke et al., 2014). This suggested that the 3D seismic data would be capable of detecting more critically-stressed faults that could be reactivated during hydraulic stimulation of future shale-gas wells.

The location of the Preston New Road wells, around 4 km south of the Preese Hall 1 well, was chosen in part to avoid major faults identified in the same 3D seismic dataset (Cuadrilla Bowland Ltd, 2019). Smaller seismic discontinuities (SDs) observed closer to the PNR wells were also considered as potential faults, although the closest SD was 300 metres away from the closest injection point and therefore considered to have a low risk of fault reactivation during hydraulic fracturing.

In the Autumn of 2018, the hydraulic fracturing stimulation of the first PNR well, PNR-1z, produced multiple "red light" events (i.e., seismic events with magnitude above M_L 0.5, which forced the operator to suspend the injection operations temporarily). Operations resumed with the operator skipping some stages to avoid a further reactivation of faults identified with microseismic observations (Clarke et al., 2019). The maximum magnitude reported during the stimulation of the PNR-1z was M_L 1.5, with the British Geological Survey reporting an intensity of 2 (i.e., scarcely felt, according to the European Macroseismic Scale -EMS). The event was felt by some members of the public living near to the well site, though the event was not strong enough to cause any disturbance or damage to the nearby communities or infrastructure.

The hydraulic fracturing stimulation of the second PNR well, PNR-2, in August 2019, also produced multiple red-light events, with a maximum magnitude 2.9 and an intensity level 6 on the same EMS scale (i.e., strong ground motions and possible minor damages to ordinary buildings). This event occurred after only seven HF stages (of 45 planned; Cuadrilla Bowland Ltd, 2019), after which the regulator ordered a shut down of injection operations, and later imposed a further moratorium on shale gas hydraulic fracturing in the UK that remains in place today.

The locations and geometries of the faults that were reactivated during stimulation of both PNR-1z and PNR-2 (Figure 2) have been constrained from observations of microseismic event locations and source mechanisms (Clarke et al., 2019a; Kettlety et al., 2021; Kettlety and Verdon, 2021). However,

these structures were not identified in interpretations of the 3D seismic dataset that were produced prior to the hydraulic fracturing operations.

The local stress regime at the PNR site has been described by Clarke et al. (2019b). The stress gradients for the Bowland Shale, located at an average depth of 2200 m for the PNR wells are S_{HMAX} = 1.4 psi/ft, S_V = 1.114psi/ft, and S_{hmin} = 0.725psi/ft (31.7, 25, and 16.4 MPa/km respectively), and assuming Andersonian stress conditions (i.e. the vertical stress -S_V- is a principal stress, and the other two are horizontal (Anderson E. M., 1951)). The vertical stress gradient (S_V) was calculated from density logs from the vertical wells in the area (particularly from the well Preese Hall 1, shown in Figure 1c), and the gradient of the minimum horizontal stress (S_{hmin}) was obtained from the Fracture Closure Pressures (FCP) measured from diagnostic fracture injection tests (DFIT) done at different depths within the Bowland shale (also from the Preese Hall 1 well). The gradient of the maximum horizontal stress (S_{HMAX}) has a higher uncertainty as it can only be constrained from the rock's internal strength, and it requires further measurements of the rock's internal friction (which can be highly variable in a formation as heterogeneous as a shale), and the implementation of a frictional faulting theory (as the Mohr-Coulomb faulting envelope, discussed in detail in the Fault Slip Potential section and in Figure 11). The S_{HMax} orientation for the studied area, measured from the breakouts observed in image logs from the Preese Hall-1 well, is approximately 173°. The pore pressure gradient is 0.58 psi/ft (13 MPa/km), which is significantly higher than a hydrostatic pressure of 0.45 psi/ft (10 MPa/km), meaning that the Bowland Shale is highly overpressured. Source mechanisms for the microseismic events showed that, for both PNR-1z and PNR-2, the largest induced events had strike-slip focal mechanisms.

Fault size and earthquake magnitude

The magnitudes of induced earthquakes will be limited by the size of the reactivated fault. Earthquake moment, M_O is defined by:

$$M_O = GAD, \quad (1)$$

where A is the rupture area, D is the average slip, and *G* is the rock shear modulus. The resulting moment magnitude, M_W, is given by:

$$M_W = \frac{2}{3}\log M_O - 6.07. \quad (2)$$

Equation (1) can be reformulated in terms of the earthquake stress drop, $\Delta\sigma$ (Kanamori and Brodsky, 2004), which is observed to be scale invariant, typically ranging between 0.01 – 100 MPa (1.45 - 14500 psi) (e.g., Abercrombie and Leary, 1993; Bohnhoff et al, 2016), such that:

$$M_O = \Delta\sigma A^{\frac{3}{2}}. \quad (3)$$

Table 1 lists the sizes of rupture (and hence the size of pre-existing fault) required for a given earthquake magnitude, assuming a stress-drop of 1 MPa (145 psi; average stress drop between 0.01 and 100 MPa, in Log_{10} scale), and a fault aspect ratio of 1 (i.e., a square rupture plane).

The geophysical detectability of a fault will primarily depend on its length and on the amount of offset that has accumulated. Faults typically display fractal (i.e., self-similar) scaling behaviour, where fault dimensions scale with fault offset (e.g., Cowie and Scholz, 1992). This occurs because both offset and length accumulate concurrently as a fault develops and grows. While this scaling between fault length and offset is observed to vary depending on tectonic settings (e.g., Anderson et al., 1996), Table 1 also lists the expected offset that would be present given a typical relationship between offset and fault length of 1 % (e.g., Dawers et al., 1993). Note that these values represent minimum fault size for a given magnitude, since they represent faults rupturing in their entirety, whereas in reality, larger faults may host smaller earthquakes if only a portion of the fault is ruptured. Nevertheless, these values serve to provide an initial constraint on our ability to mitigate HF-IS through the geophysical mapping of pre-existing faults: if typical resolution of good-quality 3D reflection seismic data is of the order of 10s of meters, then we might expect faults capable of hosting earthquakes of M 4 or lower to fall below the survey resolution.

However, fault identification in 3D seismic surveys is usually based on mapping vertical displacement of horizons. In the case of the Bowland shale area in central Britain, multiple faults with vertical offsets (i.e., normal and reverse faults) have been interpreted in regional 2D seismic images (Andrews, 2013), which has been essential to reconstruct the area's complex tectonic history. However, if the present local stress regime is of a strike-slip nature, then any induced seismicity would be expected to occur on strike-slip faults (as those interpreted from the location and focal mechanisms of the microseismic events recorded during the hydraulic stimulation of the PNR wells - Figure 3). Since these may not produce significant vertical displacement, even larger strike-slip faults may be missed when interpreting 3D seismic datasets.

3D Seismic Interpretation

We began our 3D seismic interpretation in this area by manually picking key horizons from tied wells. Calibrated with the 3D seismic data, Preese Hall-1 (PH-1), Grange Hill-1 (GH-1), and Thistleton-1 (TH-1) wells provide locations of formation tops, which can be used as the starting points for horizon picking. From there, key horizons such as the Manchester Marl Formation, Coal Measure Group, Millstone Grit Group, Upper and Lower Bowland Shale Formation, and Worston Shale Group, have been picked (see the stratigraphic column in Figure 2). In addition, the Variscan Unconformity has also been tracked across the 3D seismic volume. Preliminary fault picking based on detecting discontinuities and offsets of horizons was then used to locate faults. We note that, due to the complicated structural and tectonic setting, manual picking of horizons and faults can be challenging even in this high-quality seismic data.

Figure 4 shows the interpretation of the 3D seismic data including faults and horizons on a selection of cross-sections. The Variscan Unconformity is located below the Manchester Marl Formation and can be seen clearly cutting through the older formations below. The tectonic complexity of the strata underneath the unconformity is noticeably higher than those above, including faulting and folding in the older formations. The 3D seismic data reveals an anticline in the north-western area of the data, with its folding axis lying in the NE-SW direction. The horizons below the unconformity generally incline towards the NE, terminating against the unconformity. The identified faults can be separated into two populations. The first group consists of thrust faults which strike NE-SW and dip

in either NW or SE directions. Most of the thrust faults found in this region are located below the Variscan Unconformity. Larger normal faults are observed running through strata both above and below the unconformity. These faults can reach up to 7.5 km length. In addition to these faults, we observe large fracture zones (dark, chaotic areas shown by the blue arrows in Figure 6), where the reflection signals are much more chaotic. These zones are located mostly in the SE of the seismic data cube, with some in the N and NW.

However, the dimensions of the main faults reactivated during the hydraulic stimulations of the PNR wells, of less than 0.5 km in length (interpreted from the microseismicity observed during the stimulations, as shown in Figure 3), are much smaller than the major faults of several kilometers in length, interpreted from vertical sections of the 3D reflection seismic data (Figure 4). A close view of the same 3D seismic data near the PNR wells (Figure 5) shows that the aforementioned reactivated faults at PNR site are not clearly visible in the volume, at least from the raw seismic amplitude.

To complement this fault interpretation based on raw amplitudes, we tested multiple seismic attributes commonly implemented to enhance the detection of faults and seismic discontinuities in seismic images. In this study, similarity, spectral decomposition, and curvature have been applied to the seismic volume (Figure 6 and 7).

Introduced by Bahorich and Farmer (1995), similarity measures coherence by comparing signals between adjacent gathers using cross-correlation or semblance. A fault may create a difference in the signals between adjacent locations; thus, the similarity attribute would highlight faults as regions with low similarity. In this study, we used the similarity attribute provided by OpendTect (dGB Earth Sciences, 2015) with a calculation time gate of [-28, 28] ms. The similarity values can be calculated by the following equation:

$$sim = 1 - \frac{\sqrt{\sum_{i=1}^{N}(X_i - Y_i)^2}}{\sqrt{\sum_{i=1}^{N} X_i^2} + \sqrt{\sum_{i=1}^{N} Y_i^2}}, \quad (4)$$

where *sim* is the similarity value and X and Y are vectors of length N samples.

Spectral decomposition is a method of converting seismic signals from time domain to frequency domain using the Continuous Wavelet Transform (CWT) algorithm.

Given the wavelet $\psi(t)$,

$$CWT(\sigma, \tau) = \frac{1}{\sqrt{\sigma}} \int_{-\infty}^{\infty} f(t) \bar{\psi}\left(\frac{t-\tau}{\sigma}\right) dt, \quad (5)$$

where $\bar{\psi}$ is the complex conjugate of ψ, t is time, τ is the time translation, and σ is the dilation of the wavelet (Sinha et al., 2005). The data in frequency domain, can then be tuned to a specific frequency value to manipulate the interference of signals for highlighting geological features. Different geological features have different tuning behaviours since the interference is influenced by local distribution of the impedance contrasts and the wavelet. For example, faults with different sizes and locations would tune in or tune out at different frequencies. Therefore, it is commonly utilized for identifying lateral changes or discontinuities on a surface. In practice, the spectral decomposition attribute is commonly used with RGB-colour blending. The attribute volumes are computed using 3 different tuning frequencies: 15, 30, and 75 Hz (translating to low, mid, and high frequency ranges,

respectively). These are represented by different colour schemes (red, green, and blue in order). Then, they can be overlapped and displayed together as one attribute, which can improve the accuracy of the results and interpretations.

Finally, the curvature attribute indicates the rate of change of dip of a surface. In other words, it is a measure of how deformed or bent a particular point of a surface is. A curvature value (K) of a surface can be calculated by using the following equation:

$$K = \frac{d^2y/dx^2}{(1+(dy/dx)^2)^{3/2}}, \quad (6)$$

where x and y are the variables in the quadratic equation that represents the surface or curve (Roberts, 2001). Positive curvature values represent antiform features, while negative values represent synform features. Thus, the curvature attribute can be used to detect features that offset a surface, or to enhance the relief of geological features. In three dimensions, the curvature is calculated from two perpendicular vertical planes, referred to as normal curvatures, composing of maximum and minimum curvatures. The maximum curvature is a measure of the maximum bending of a surface at the given point, while the minimum curvature measures the curve perpendicular to the maximum curvature. The maximum curvature is typically utilized in fault detection. There are various ways of displaying curvature, including mean curvature, Gaussian curvature, most-positive curvature, most-negative curvature, dip curvature, and strike curvature, though most-positive and most-negative curvatures are the most convenient to use to detect geological features (Chopra & Marfurt, 2007). Most-positive and most-negative curvature attributes calculate the most positive and most negative values from the normal curvature.

In addition to tracking these three seismic attributes (similarity, spectral decomposition, and curvature) across the horizons shown in Figure 4 (results of which are shown in Figure 6), we pick additional sub-horizons sh-A and sh-B around the PNR wells (the results of which are shown in Figure 7). These sub-horizons run through the centres of the microseismic clouds generated during stimulation of PNR-1z and PNR-2, and as such should be optimally positioned to identify the re-activated faults.

The similarity attribute is able to pick up both groups of faults (normal and thrust) described above, represented by black lines or dissimilarities in Figure 6a, 7a, and 7b. Likewise, the spectral decomposition attribute (Figure 6b, 6c, 7c, 7d, 7e, and 7f), especially at higher frequencies. The curvature attributes display some features which do not show up on the similarity and spectral decomposition attributes. These are represented by continuous lines of high or low curvature values in Figure 7g and h. Our interpretation is that these geological features are offsets from faults and remnants of ancient channels.

However, none of attributes are able to confidently and unambiguously identify the reactivated faults near the PNR site (Figure 7). Although the similarity and spectral decomposition attributes cannot directly pick up these faults, they can detect some evidence which could be used to infer the presence of the faults. The similarity and spectral decomposition attributes can pick up geological features (red, dashed rectangles in Figure 8) which terminate at the location of the PNR-1z fault plane identified by Clarke et al. (2018), perhaps indicating the offset of geological features. The high frequency component of the spectral decomposition attribute can detect faint dark lines (white,

dashed rectangles in Figure 8) near the location of the fault planes proposed by Clarke et al. (2019) and Kettlety et al. (2021a). Nevertheless, without prior knowledge of the fault plane locations from microseismic observations, these faint features are not distinguishable above the typical background variability observed across the section. As such, we conclude that these seismic attributes are still not capable of reliably detecting the causative faults at PNR-1z and PNR-2 wells.

Automatic Fault Interpretation

To complement the manual, and attribute-assisted, 3D seismic interpretation, a Thinned Fault Likelihood (TFL) attribute was calculated for the same dataset to detect fault surfaces automatically. This TFL is based on a semblance attribute, and therefore is also a coherence measurement between seismic traces (varying between 0 and 1). Then, a structure-oriented filter is applied to thin the fault likelihood, to generate fault images with higher resolution when compared with conventional discontinuity attributes as semblance or curvature (Hale, 2013).

Hundreds of faults are clearly visible from the TFL attribute calculated from the 3D seismic (Figure 9). To extract the geometry of the fault planes (i.e., centre location, length and azimuth), observed from the TFL attribute, we used the Standard Hough Transform (SHT) which is a feature extraction algorithm commonly implemented as part of image processing and computer vision workflows to extract analytically defined shapes, as circles or lines (the simplest case of the Hough transform), from images. This SHT method first calculates the edges from the input image to obtain a binary version (black and white background from Figure 10a), and then uses the parametric equation of a line:

$$\rho = x*\cos(\theta) + y*\sin(\theta), \quad (7)$$

where ρ is the perpendicular distance from the origin to the line, and θ is the angle of the perpendicular projection to the line, also from the origin. The SHT transforms the binary image into the ρ-θ domain (Figure 10b), where each peak extracted from the ρ-θ image corresponds to one line (shown in green back in Figure 10a).

Of the faults identified by the TFL attribute (Figure 9), some are compatible with the major faults identified in the manual geological interpretation described above (Figure 4). Some NE-SW striking faults with high "likelihood" (i.e., TFL closer to 1) are identified. Their location and orientation are close to that observed for the 2011 M_L = 2.3 earthquake that was triggered during stimulation of the Preese Hall well (Clarke et al., 2014). However, fewer faults are observed around the PNR wells, and no structures that match the locations and focal plane orientations of the 2018 M_L = 1.5 and 2019 M_L = 2.9 induced earthquakes.

The length of the extracted fault lines varies between 0.4 and 1.8 km (with the shortest fault length of 0.4 km corresponding roughly to a seismic event of magnitude 3.0 - see Table 1). These lengths confirm one of the issues of using 3D seismic data to guide site selection to mitigate induced seismicity: faults of sufficient size to cause M_L 3.0 earthquakes may be at the very limit of survey resolution. While such events are unlikely to be of sufficient size to cause any significant damage (e.g., Nievas et al., 2020), since they occur at relatively shallow depths, they may be felt by people nearby, leading to significant public unease with the causative industries.

Fault Slip Potential

Once the fault lines are extracted from the TFL attribute from the 3D seismic survey, their fault slip potential (FSP) can be estimated by integrating them with the formation stress and pore pressure gradients. This FSP analysis is commonly done by integrating the effective normal and shear stress, the fault planes, and a failure boundary in a Mohr diagram (Walsh and Zoback, 2016; Walsh et al, 2018), as shown in Figure 11b. To do so, first, the effective normal stresses (σ) must be calculated by subtracting the reservoir's pore pressure. At the depth of the horizontal section of the PNR wells (shown in Figure 3c), of approximately 2200 meters (7218 ft), and with stress gradients of S_{HMAX} = 1.4 psi/ft, S_V = 1.114psi/ft, and S_{hmin} = 0.725psi/ft, and a pore pressure gradient (Pp) of 0.58 psf/ft, the effective normal stresses are

σ_H = Depth * (S_{HMAX} – Pp) = 7218 ft * (1.4 psi/ft - 0.58 psi/ft) = 5919 psi, (8)

σ_V = Depth * (S_V – Pp) = 7218 ft * (1.114 psi/ft - 0.58 psi/ft) = 3854 psi, and (9)

σ_h = Depth * (S_{HMAX} – Pp) = 7218 ft * (0.725 psi/ft - 0.58 psi/ft) = 1047 psi. (10)

From these normal stresses, the shear stress (τ) can be calculated for any fault orientation from a 3D Mohr diagram, by calculating three Mohr circles centered between the normal stresses and at a shear stress of zero (Figure 11b). Then, each fault plane obtained from the 3D seismic dataset in the Bowland is plotted inside the same Mohr circles from their orientation relative to the orientation of the maximum horizontal stress, of 173° in this area. Then, we measure the distance between each fault plane (i.e., each do inside the Mohr circles) and a failure function (as the red line shown in Figure 11b), which corresponds to the additional pore pressure required to fail (i.e., to slip). In this study we used a linear Coulomb Failure Function, where $\tau=\mu\sigma$, and friction coefficient (μ) of 0.75 that was first estimated for this area (Clarke et al., 2019). However, this friction coefficient, that typically ranges between 0.6 and 1.0, can be highly variable in a formation as heterogeneous and highly fractured as the Bowland shale, and the additional pore pressure required for each fault line to reach the failure envelope, varies significantly depending on the friction coefficients.

We find that several of the identified faults surpass the Mohr-Coulomb failure threshold (red line in Figure 11b) meaning that they are critically stressed, due to their optimal orientation relative to the maximum horizontal stress (Figure 11c and d), and the high pore pressure that significantly reduces the effective normal stresses. The abundance of critically stressed faults in the Bowland Shale likely explains why all wells that have been hydraulically fractured in this formation generated induced seismicity. Also, many smaller fractures in the same formation, that were undetected from the 3D seismic dataset in the Bowland shale, could also be critically stressed, which can cause wellbore stability issues while drilling the wells, as reported for the vertical wells drilled in the area (as Preese Hall 1 well shown in Figure 1c; Clarke et al., 2019).

Hydraulic fracturing for shale gas is currently subject to an ongoing moratorium in the UK, although we note that no such moratorium exists for similar activities such as geothermal stimulation (which has produced similar levels of induced seismicity, e.g., Holmgren and Werner, 2021), and for smaller-

scale hydraulic fracturing in conventional reservoirs, which has been conducted in the UK for decades, with no cases of induced seismicity recorded (Mustanen et al., 2017). Similarly, hydraulic fracturing in offshore fields in the North Sea is not under moratorium. Based on our findings here, future work would be well-directed to investigating the relative abundance of faulting, and the in-situ stress conditions, across the wider Bowland Shale formation, as areas with lower abundance of faulting and lower shear stresses may be less prone to induced seismicity. However, it should be recognized that faults of sufficient size to generate M_L 3.0 earthquakes, which will be strongly felt by nearby people, may be below the limits of seismic resolution. As such, pro-active decision making based on real-time microseismic observations (e.g., Clarke et al., 2019; Verdon and Bommer, 2021), will be required.

Conclusions

A detailed structural interpretation of an unconventional reservoir, based on multiple exploration datasets including well logs and 2D and 3D seismic surveys, is an essential step required to determine an optimum well location and design of hydraulic-fracturing stimulations, especially in areas prone to induced seismic activity such as the Bowland Shale. The Preston New Road wells near Blackpool, hydraulically fractured in 2018 and 2019, generated multiple "red-light" seismic events, including a M_L 2.9 event in August 2019. Analysis and interpretation of the 3D seismic dataset did not show any large faults (or seismic discontinuity) near these wells, and the faults were only visible from the microseismicity recorded with downhole arrays during the hydraulic stimulations. We tested multiple seismic attributes to complement the manual seismic interpretation of the main horizons and faults from the same 3D seismic dataset, observing a high structural complexity below the Variscan Unconformity.

To complement this manual seismic interpretation, we tested an automated fault detection method based on a high-resolution coherence attribute, and analyzed the slip potential of faults that were identified. This method allowed the detection of numerous critically-stress faults in the Bowland Shale with a minimum fault length of 0.4 km (potential for magnitude 3 earthquake, approximately), some of them near the hydraulic fractured wells in Preese Hall and Preston New Road and with similar orientations to the nodal planes reported for the largest-magnitude seismic events detected near each well. This method could also be implemented to evaluate possible locations of future unconventional wells that require similar hydraulic-fracturing stimulations, by avoiding critically stressed faults that could trigger anomalously high seismic activity. However, it is also clear that multiple strike-slip faults could go undetected if they are shorter than the minimum fault length detected, or if they have a very low vertical displacement, some of which could also be critically stressed if they are optimally oriented relative to the maximum horizontal stress.

Even if the application of the TFL and the FSP in the Bowland Shale does not reliably pick up strike-slip faults, it still shows a great potential that both methods can possibly improve the drilling site selection and operation planning. The ability to better detect faults and calculate probability of each fault to rupture is essential since avoiding critically stressed faults will tremendously reduce the chance of triggering HF-IS. Furthermore, these processes are performed before the drilling, meaning that operators can manage the problem before it actually occurs, unlike the TLS. We predict that, combining with the traditional, manual methods, the improved TFL and FSP will play a significant

role in risk assessments of unconventional explorations in the future, not only for the Bowland Shale, but for other regions as well.

Acknowledgements

We thank the UK Onshore Geophysical Library (UKOGL) for supplying the 3D seismic dataset analysed in this case study, and dGB Earth Sciences for supplying an academic license of OpendTect Pro used for the interpretation of the same 3D seismic dataset from the Bowland Shale. The microseismic datasets of the PNR wells were made publicly available by the UK Oil and Gas Authority. This study is a product of the Bristol University Microseismicity Projects (BUMPS) group.

References

Abercrombie, R., & Leary, P. (1993). Source parameters of small earthquakes recorded at 2.5 km depth, Cajon Pass, southern California: Implications for earthquake scaling. *Geophysical Research Letters, 20*(14), 1511-1514.

Anderson, E. M. (1951). *The Dynamics of Faulting and Dyke Formation with Applications to Britain.* Edinburgh: Oliver and Boyd.

Anderson, I., & Underhill, J. R. (2020). Structural constraints on Lower Carboniferous shale gas exploration in the Craven Basin, NW England. *Petroleum Geosciences, 26*, 303–324. doi:https://doi.org/10.1144/petgeo2019-125

Anderson, J. G., Wesnousky, S. G., & Stirling, M. W. (1996). Earthquake size as a function of fault slip rate. *Bulletin of the Seismological Society of America, 86*(3), 683–690.

Andrews, I. (2013). The Carboniferous Bowland Shale gas study: geology and resource estimation. *British Geological Survey for Department of Energy and Climate Change*.

Bahorich, M., & Farmer, S. (1995). 3-D seismic discontinuity for faults and stratigraphic features: The coherence cube. *The Leading Edge, 14*(10), 1053-1058.

Bohnhoff, M., Kwiatek, G., & Dresen, G. (2016). Von der Gesteinsprobe bis zur Plattengrenze: Skalenübergreifende Analyse von Bruchprozessen. *System Erde, 6*(1), 50-55.

Chopra, S., & Marfurt, K. (2007). Seismic curvature attributes for mapping faults/fractures, and other stratigraphic features. *Recorder, 32*(9), 37-41. Retrieved from https://csegrecorder.com/articles/view/seismic-curvature-attributes-for-mapping-faults-fractures-and-other

Clarke, H., Eisner, L., Styles, P., & Turner, P. (2014). Felt seismicity associated with shale gas hydraulic fracturing: The first documented example in Europe. *Geophysical Research Letters, 41*(23), 8308–8314. doi:https://doi.org/10.1002/2014GL062047

Clarke, H., Soroush, H., & Wood, T. (2019). SPE-195563-MS. Preston New Road: The Role of Geomechanics in Successful Drilling of the UK's First Horizontal Shale Gas Well. *SPE Europec featured at 81st EAGE Conference and Exhibition. London, England, UK, 3-6 June 2019.*

Clarke, H., Turner, P., Bustin, R. M., Riley, N., & Besly, B. (2018). Shale gas resources of the Bowland Basin, NW England: a holistic study. *Petroleum Geoscience, 24*, 287–322. doi:https://doi.org/10.1144/petgeo2017-066

Clarke, H., Verdon, J. P., Kettlety, T., Baird, A. F., & Kendall, J.-M. (2019). Real-Time Imaging, Forecasting, and Management of Human-Induced Seismicity at Preston New Road, Lancashire, England. *Seismological Research Letters, 90*(5), 1902–1915. doi:https://doi.org/10.1785/0220190110

Cowie, P. A., & Scholz, C. H. (1992). Displacement-length scaling relationship for faults: data synthesis and discussion. *Journal of Structural Geology, 14*(10), 1149-1156 .

Cuadrilla Bowland Ltd. (2019). *Hydraulic Fracture Plan PNR 2.* Retrieved May 2021, from https://consult.environment-agency.gov.uk/onshore-oil-and-gas/information-on-cuadrillas-preston-new-road-site/user_uploads/pnr-2-hfp-v3.0.pdf

Dawers, N. H., Anders, M. H., & Scholz, C. H. (1993). Growth of normal faults: Displacement-length scaling. *GeologySearch, 21*(12), 1107–1110.

Hale, D. (2013). Methods to compute fault images, extract fault surfaces, and estimate fault throws from 3D seismic images. *Geophysics, 78*(2), O33–O43. doi:https://doi.org/10.1190/geo2012-0331.1

Holmgren, J. M., & Werner, M. J. (2021). Raspberry Shake Instruments Provide Initial Ground-Motion Assessment of the Induced Seismicity at the United Downs Deep Geothermal Power Project in Cornwall, United Kingdom. *The Seismic Record, 1*(1), 27–34.

Kendall, J.-M., Butcher, A., Stork, A. L., & Verdon, J. P. (2019). How big is a small earthquake? Challenges in determining microseismic magnitudes. *First Break, 37*(2), 51 - 56. doi:https://doi.org/10.3997/1365-2397.n0015

Kettlety, T., & Verdon, J. P. (2021). Fault Triggering Mechanisms for Hydraulic Fracturing-Induced Seismicity From the Preston New Road, UK Case Study. *Frontiers in Earth Science, 9*. doi:https://doi.org/10.3389/feart.2021.670771

Kettlety, T., Verdon, J. P., Butcher, A., Hampson, M., & Craddock, L. (2021). High-Resolution Imaging of the ML 2.9 August 2019 Earthquake in Lancashire, United Kingdom, Induced by Hydraulic Fracturing during Preston New Road PNR-2 Operations. *Seismological Research Letters, 92*(1), 151–169. doi:https://doi.org/10.1785/0220200187

Kwiatek, G., Saarno, T., Ader, T., Bluemle, F., Bohnhoff, M., Chendorain, M., . . . Passmore, P. (2019). Controlling fluid-induced seismicity during a 6.1-km-deep geothermal stimulation in Finland. *Science*. doi:10.1126/sciadv.aav7224

Nievas, C. I., Bommer, J. J., Crowley, H., & Elk, J. v. (2020). Global occurrence and impact of small-to-medium magnitude earthquakes: a statistical analysis. *Bulletin of Earthquake Engineering, 18*, 1–35.

OGA. (2019). *Interim report of the scientific analysis of data gathered from Cuadrilla's operations at Preston New Road.* UK Oil and Gas Authority.

Othman, A. A., Fathy, M., & Maher, A. (2016). The use of spectral decomposition technique for delineation of channels at Solar gas discovery, offshore West Nile Delta, Egypt. *Egyptian Journal of Petroleum, 25*(1), 45-51. doi:10.1016/j.ejpe.2015.03.005

Roberts, A. (2001). Curvature attributes and their application to 3D interpreted horizons. *First Break, 19*(2), 85-100.

Shapiro, S. A., Krüger, O. S., Dinske, C., & Langenbruch, C. (2011). Magnitudes of induced earthquakes and geometric scales of fluid-stimulated rock volumes. *Geophysics, 76*(6), WC55–WC63. doi:https://doi.org/10.1190/geo2010-0349.1

Sinha, S., Routh, P. S., Anno, P. D., & Castagna, J. P. (2005). Spectral decomposition of seismic data with continuous-wavelet transform. *Geophysics, 70*(6), 19-25.

Smith, N., Turner, P., & Williams, G. (2010). UK data and analysis for shale gas prospectivity. In B. Vining, & S. Pickering, *Petroleum Geology : From Mature Basins to New Frontiers : Proceedings of the 7th Petroleum Geology Conference* (pp. 1087-1098). Geological Society of London. Retrieved from http://nora.nerc.ac.uk/id/eprint/13090/

Verdon, J. P., & Bommer, J. J. (2021). Green, yellow, red, or out of the blue? An assessment of Traffic Light Schemes to mitigate the impact of hydraulic fracturing-induced seismicity. *Journal of Seismology, 25*, 301–326. doi:https://doi.org/10.1007/s10950-020-09966-9

Walsh, F. R., & Zoback, M. D. (2016). Probabilistic assessment of potential fault slip related to injection-induced earthquakes: Application to north-central Oklahoma, USA. *Geology, 44*(12), 991–994.

Walsh, R., Zoback, M. D., Lele, S. P., Pais, D., Weingarten, M., & Tyrrell, T. (2018). FSP 2.0: A Program for Probabilistic Estimation of Fault Slip Potential Resulting from Fluid Injection. Retrieved from https://scits.stanford.edu/fault-slip-potential-fsp

Wesnousky, S. G. (1988). Seismological and structural evolution of strike-slip faults. *Nature*(335), 340–343.

Figures Caption

Figure 1. Bowland shale area in central Great Britain (a) with the 2D and 3D seismic exploration surveys (b) acquired for exploration of conventional oil and gas fields, coal and coalbed methane, and more recently for unconventional shale gas. The top view of the Bowland-12 3D reflection seismic data near Blackpool (c) shows the location of the wells hydraulic-fractured (to date) in the Bowland shale (first Preese Hall 1 in 2011, followed by the wells in Preston New Road, PNR, in 2018 and 2019), and a time slice of the 3D seismic data at 1260 milliseconds (just below the two PNR wells, with their depths converted to two-way-travel time), with a distance of 25 meters between in-lines and cross-lines. The microseismic events observed during the hydraulic stimulations of the PNR wells are shown in detail in Figure 3 and 5, and the structural interpretation of the vertical cross-sections are shown in Figure 4.

Figure 2. Stratigraphic column of the Bowland Basin from Carboniferous to Triassic periods. Key formations interpreted in the seismic reflection dataset (shown in Figure 4) are highlighted in the Lithostratigraphic column, as the Bowland Shale Formation (highlighted in light blue), and the Variscan Unconformity (highlighted in light brown).

Figure 3. Top, side, and front view (a, b and c respectively) of the microseismic events observed during the hydraulic-fracturing stimulations of the Preston New Road wells PNR-1z and PNR-2 (in British National Grid coordinates – BNG), recorded with temporary, multi-component downhole monitoring arrays (Clarke et al., 2019), with two nearly-vertical fault zones interpreted from the location and focal mechanism of the largest-magnitude events, both with dip angles higher than 70° (Kettlety and Verdon, 2021). The depth distribution of

the microseismic events (d) shows little overlapping of the seismicity associated with each PNR well, despite having similar magnitude ranges (e).

Figure 4. Structural interpretation of the cross-sections from the 3D seismic data shown in Figure 1c. A close view of the 3D reflection seismic data from the red, dashed rectangle in d) with the microseismic events from the hydraulic fracturing stimulations of the PNR wells shown in Figure 3, is shown in detail in Figure 5.

Figure 5. Close front and top view (a and b respectively) of a time slice and inline section of the 3D reflection seismic data shown in Figure 1 and 3, and the microseismic events observed during the hydraulic-fracturing stimulations of the Preston New Road wells PNR-1z and PNR-2 (also shown in Figure 3a and c), on top of the same 3D seismic data (c and d respectively). The yellow horizon shown in the front views (a and c) corresponds to the interpreted top of the Lower Bowland Shale.

Figure 6. Similarity and spectral decomposition attributes applied on the time slice at 1260 ms. (a) similarity attribute. (b) color-blended spectral decomposition attribute (red component is 15 Hz, green component is 30 Hz, and blue component is 75 Hz). (c) High-frequency spectral decomposition attribute (75 Hz). The orange and red lines represent the PNR-1z and PNR-2 well tracks. The blue arrows show the locations of the fracture zones, represented by areas with chaotic dark lines. These fracture zones are mostly oriented in the NE-SW direction.

Figure 7. The application of similarity, spectral decomposition, and curvature attributes on causative fault investigation at the PNR site. (a) Similarity attribute applied on the sub-horizon sh-A. (b) Similarity attribute applied on the sub-horizon sh-B. (c) Colour-blended spectral decomposition attribute applied on sub-horizon sh-A (red component is 15 Hz, green component is 30 Hz, and blue component is 75 Hz). (d) Colour-blended spectral decomposition attribute applied on sub-horizon sh-B. (e) High-frequency spectral decomposition attribute (75 Hz) applied on sub-horizon sh-A. (f) High-frequency spectral decomposition attribute (75 Hz) applied on sub-horizon sh-B. (g) Most-positive curvature attribute applied on sub-horizon sh-A. (h) Most-positive curvature attribute applied on sub-horizon sh-B. The orange and red lines represent the PNR-1z and PNR-2 well tracks.

Figure 8. (a) High-frequency (75 Hz) spectral decomposition attribute on the picked horizon near PNR-1z events. The red-dashed box corresponds to the zoomed-in views shown in b, c. and d. (b) Zoomed-in high-frequency (75 Hz) spectral decomposition attribute on the picked horizon near PNR-1z events, with the actual microseismic event locations (yellow dots) shown in (c), and with the fault plane proposed by Clarke et al. (2019) based on the same microseismic events, shown in (d). (e) High-frequency (50 Hz) spectral decomposition attribute on the picked horizon near PNR-2 events. The red-dashed box corresponds to the zoomed-in views shown in f, g. and h. (f) Zoomed-in high-frequency (50 Hz) spectral decomposition attributes on the picked horizon near PNR-2 events with the actual microseismic event locations (orange dots) shown in (g), and with the fault plane proposed by Kettlety & Verdon (2021) based on the same microseismic events, shown in (h). The yellow, dashed boxes in b, d, f, and h indicate dark lines that are believed to be the causative faults. The cyan, dashed boxes in f and h represent the geological features that potentially get cut off by the fault. The orange line represents the PNR-1z well track, while the red line represents the PNR-2 well track.

Figure 9. The Thinned Fault Likelihood attribute (TFL) from the Bowland-12 3D seismic dataset (time slice at 1200 ms, just below the PNR wells as shown in Figure 4d), shows a comprehensive understanding of the fracture network present in the Bowland Shale at 3D seismic-resolution scales (see the fault-length ranges obtained in Figure 10c), that is compatible with the previous geological interpretations of major faults (black solid lines) shown in vertical sections of the same 3D seismic dataset (Figure 4). The highlighted inset with the microseismic events observed during the hydraulic stimulations of the PNR wells, is shown in detail in Figure 3, with the same vertical and horizontal slices of the 3D seismic dataset near the PNR wells shown in Figure 5.

Figure 10. a) Binary image of the TFL shown in Figure 9 (black and white background), and the extracted fault lines from the Standard Hough Transform (SHT) are shown in green. (b) Hough transform of the binary image shown in a), in the ρ-θ domain. The extracted fault lengths range from 0.4 km to 1.8 km (c), and the largest faults have an approximate NE-SW orientation (d).

Figure 11. a) Fault Slip Potential (FSP) of the fault lines at 1200 ms interpreted from the TFL attribute (Figure 9) and extracted from a 2D standard Hough transform (Figure 10), just below the PNR wells (PNR-1Z and PNR-2) hydraulic-fractured in 2018 and 2019 respectively. The color code for each fault corresponds to the increase in pore pressure (ΔP_P) required in each fault to reduce their effective stress and reach the Mohr-Coulomb failure envelope (red line shown in b), and therefore to slip. In the linear failure envelope used in this study, where $\tau=\mu\sigma$, a friction coefficient (μ) of 0.75 was first estimated for this area (Clarke et al., 2019). However, this friction coefficient, that typically ranges between 0.6 and 1.0, can be highly variable in a formation as heterogeneous and highly fractured as the Bowland shale, and the additional pore pressure required for each fault line to reach the failure envelope, varies significantly depending on the friction coefficients. These pore pressures calculated the same fault lines, can also range from zero (as several faults are already reaching in some cases the Mohr-Coulomb failure envelope with μ=0.75, meaning that they're critically stressed) to more than 1000 psi. The orientation of these critically-stressed faults (shown in c) and d) in the normal composite and stereonet projection respectively) are also optimally oriented for a strike-slip faulting mechanism relative to the maximum horizontal stress (S_{HMax}).

Figure 1

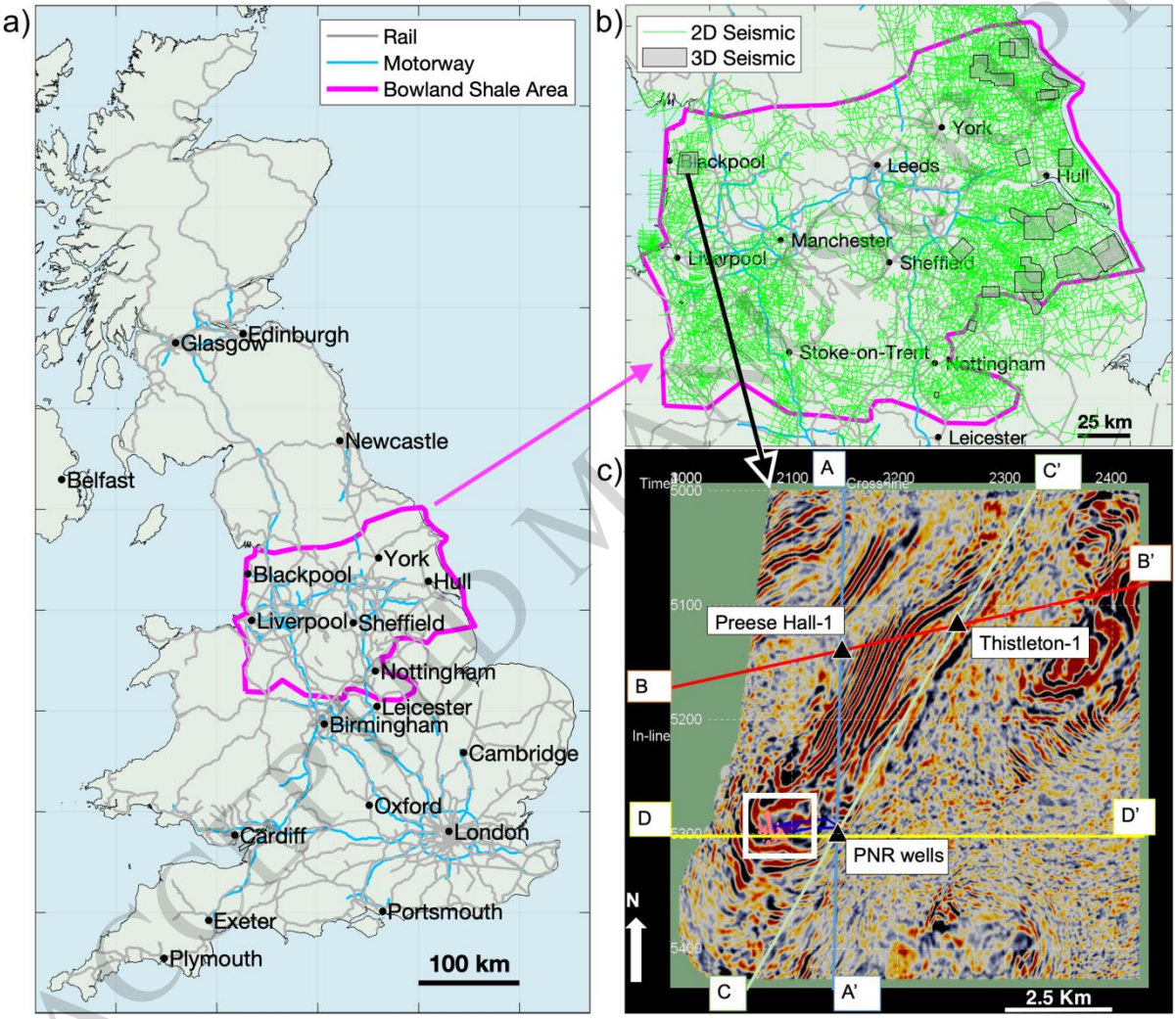

Figure 2

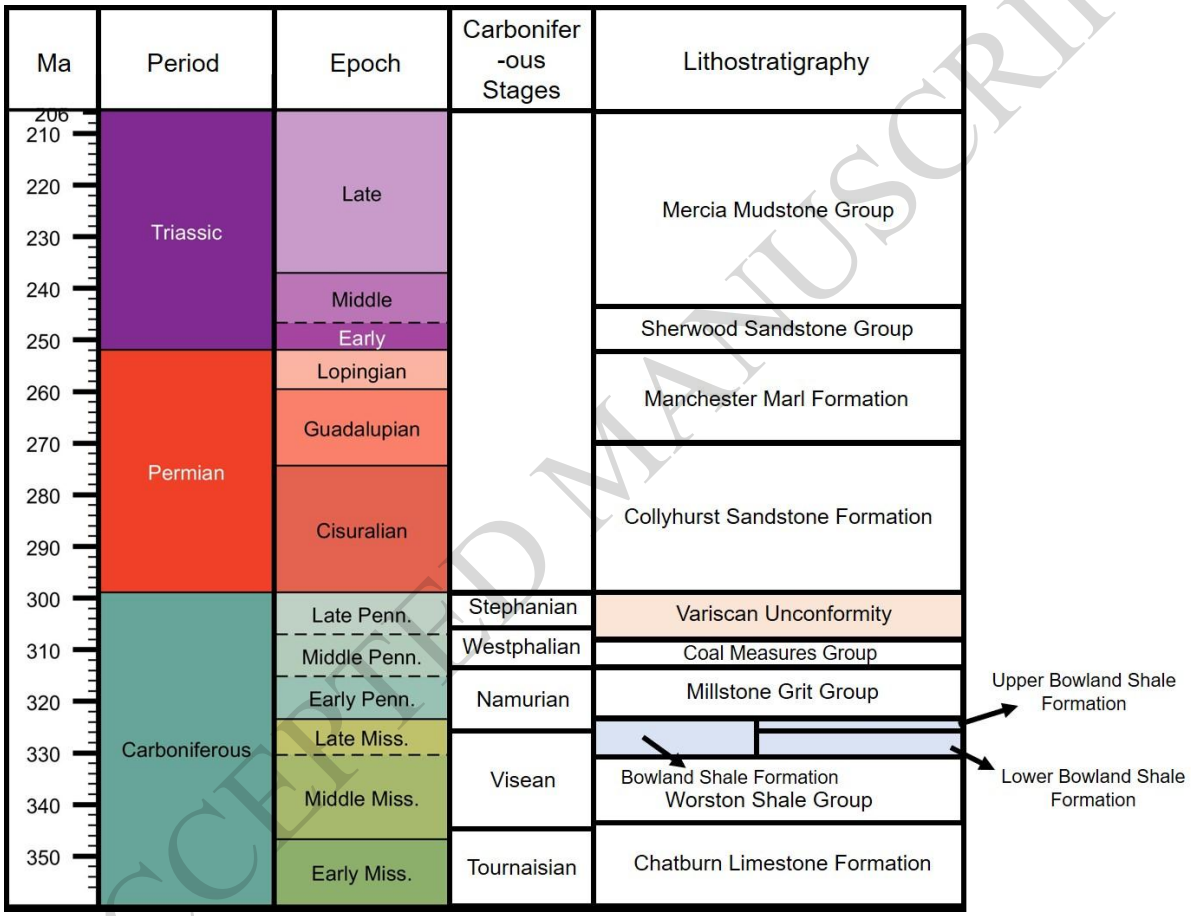

Figure 3

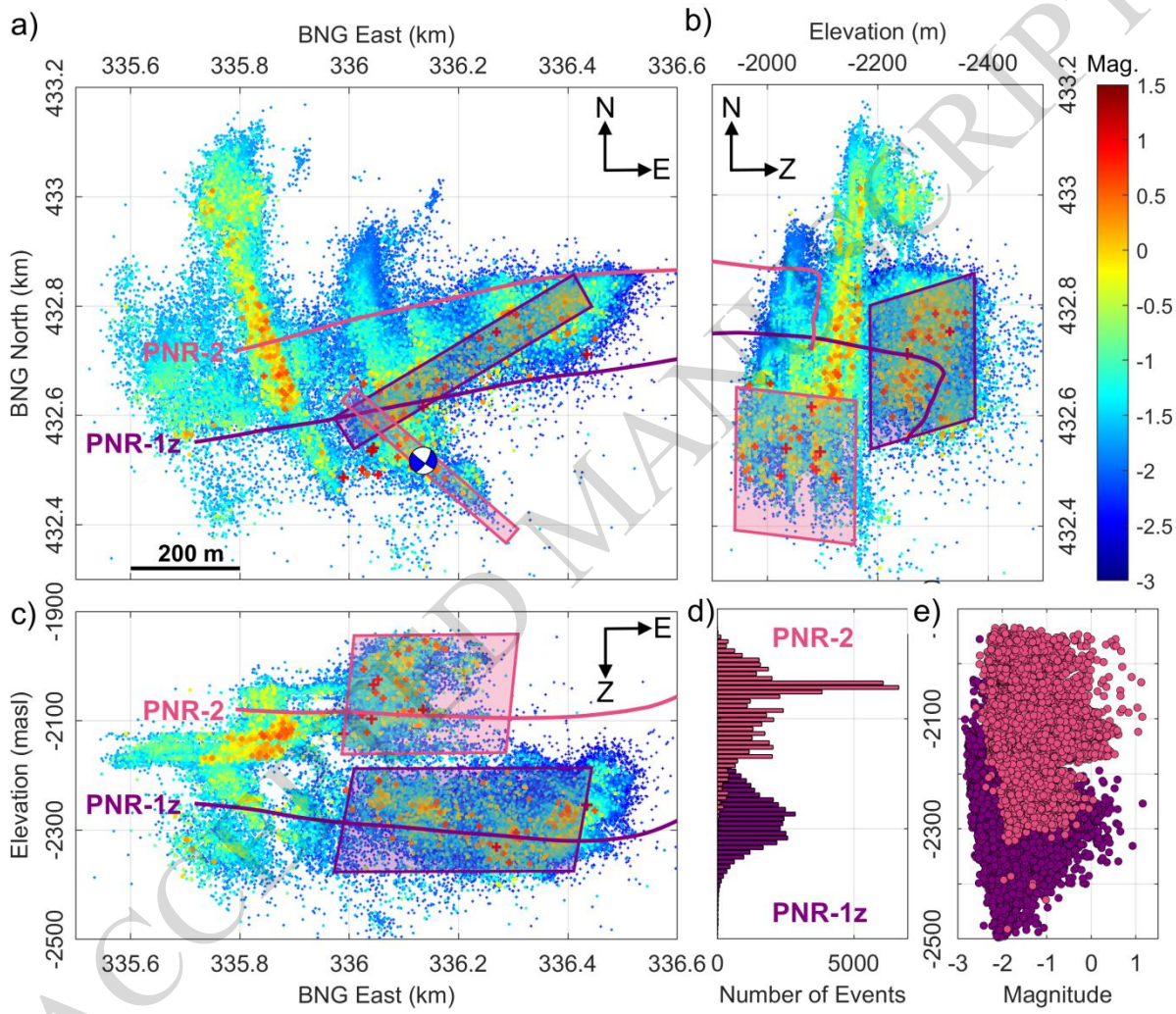

Figure 4

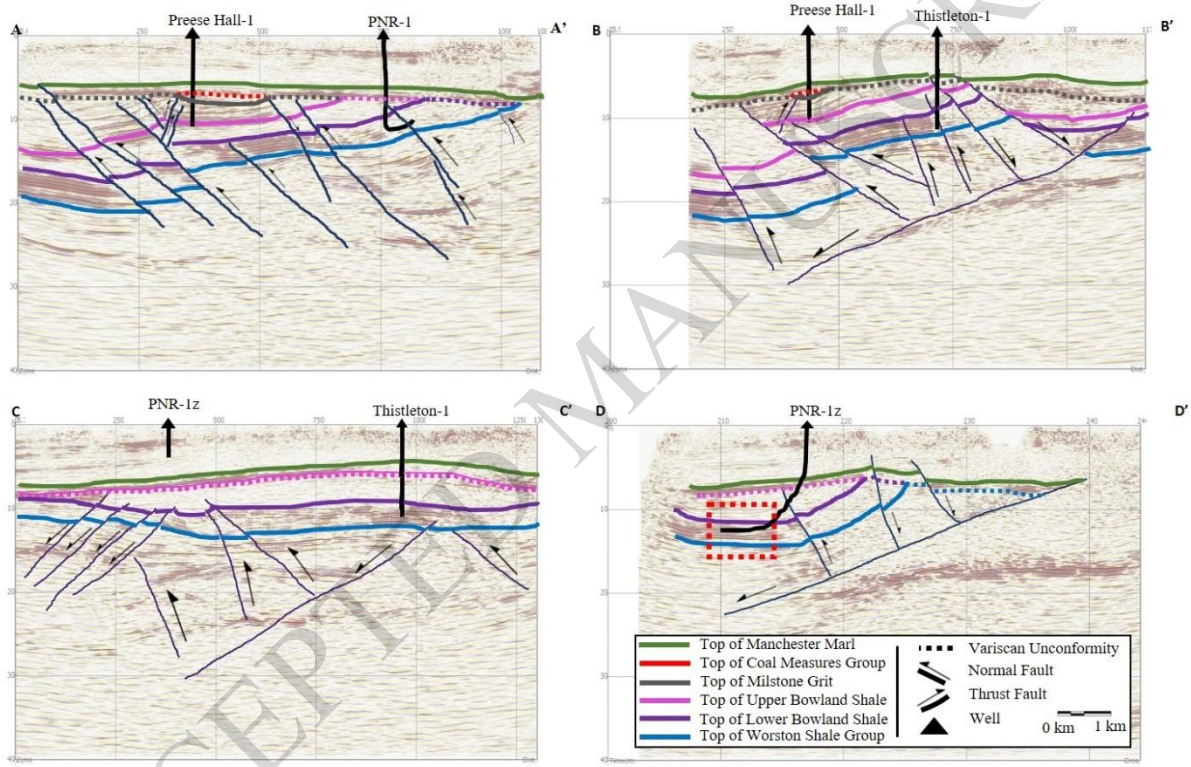

Figure 5

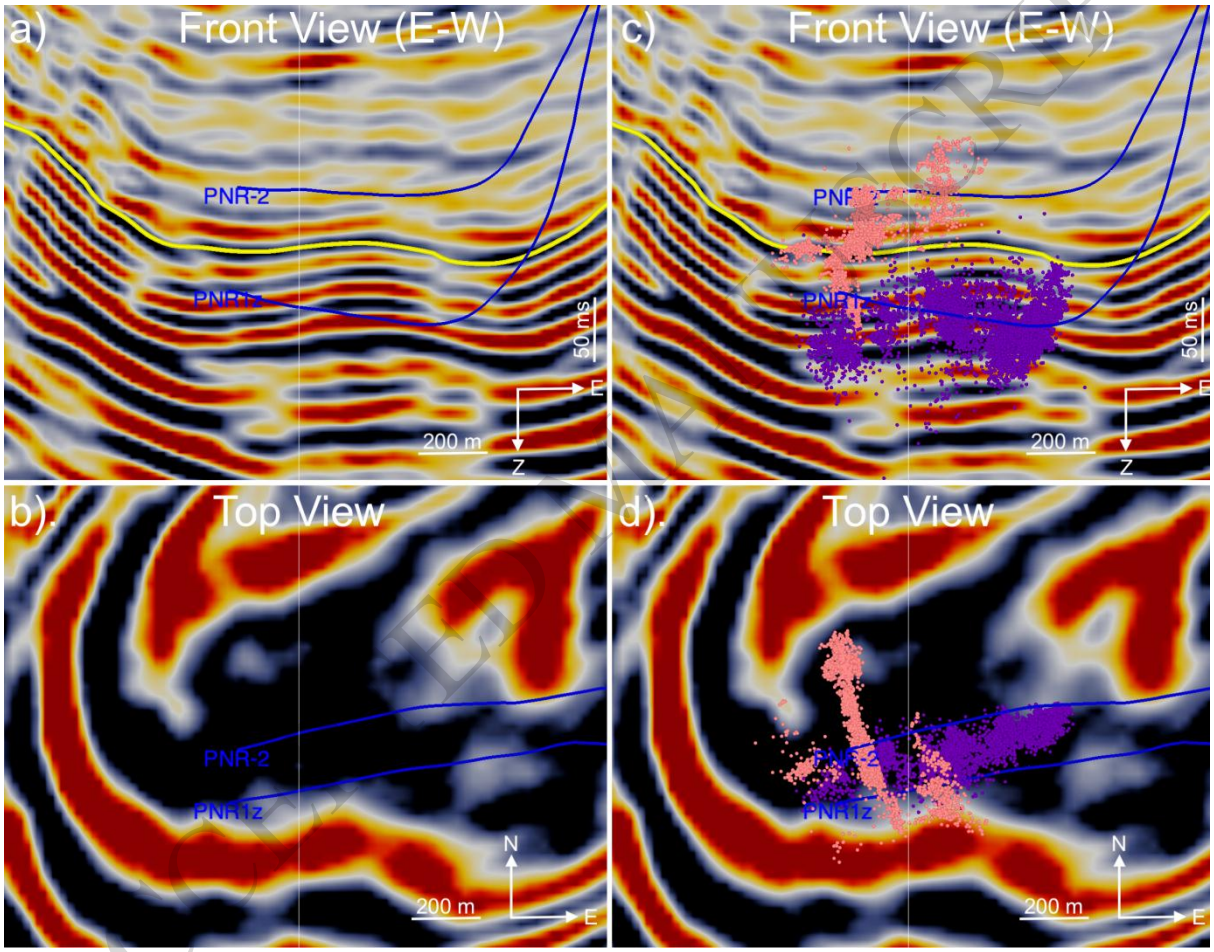

Figure 6

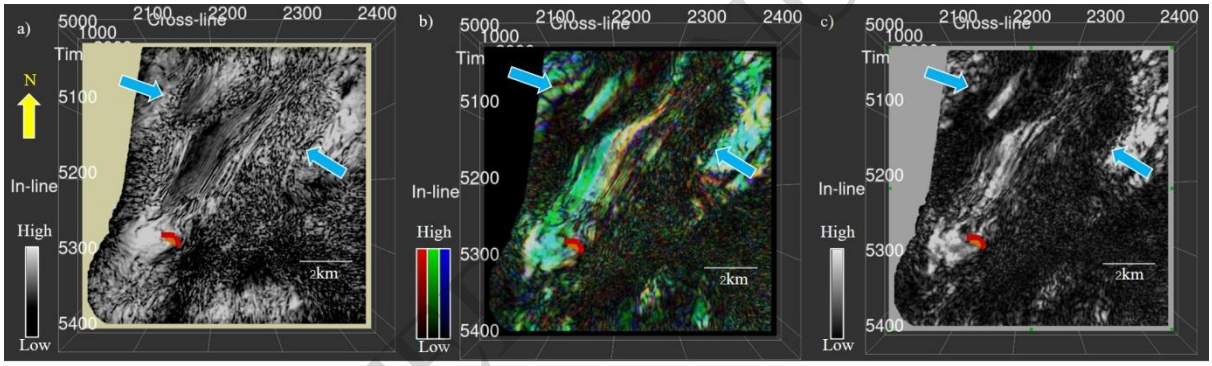

Figure 7

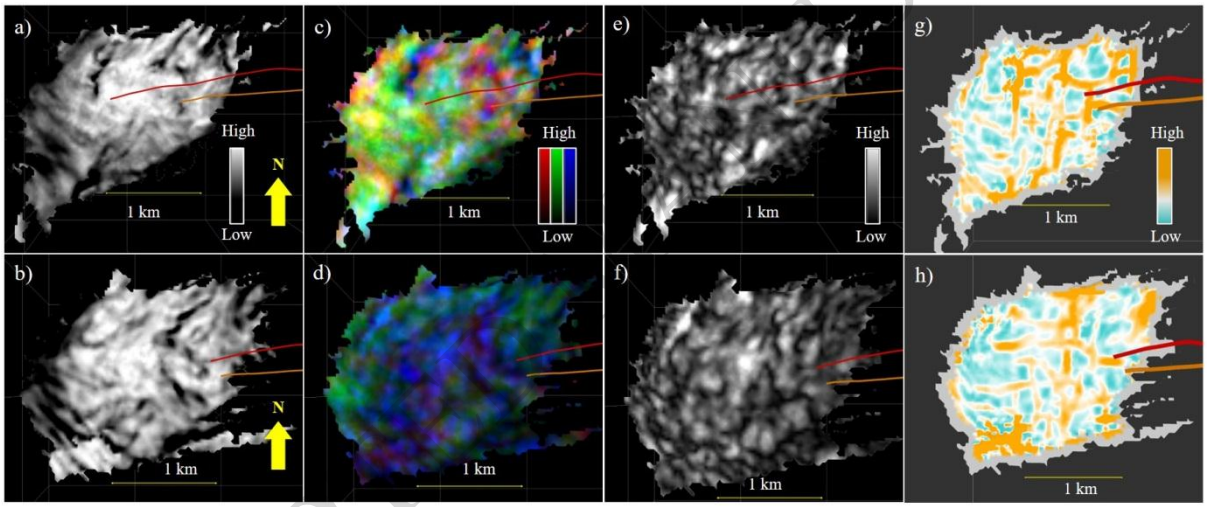

Figure 8

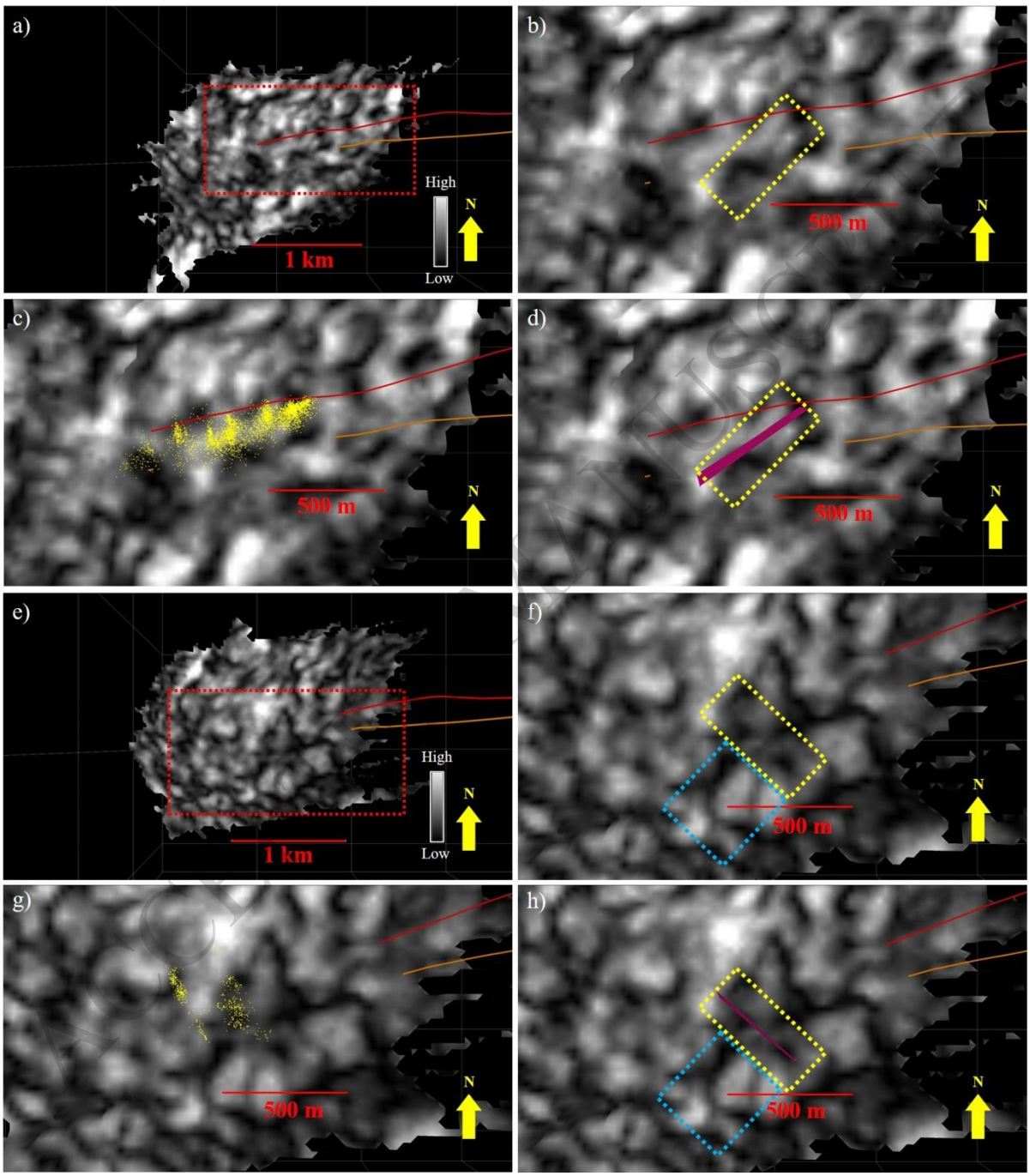

Figure 9

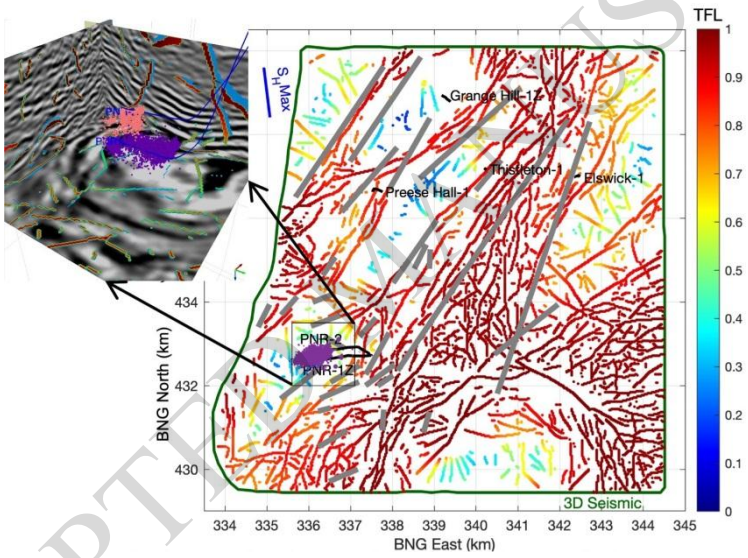

Figure 10

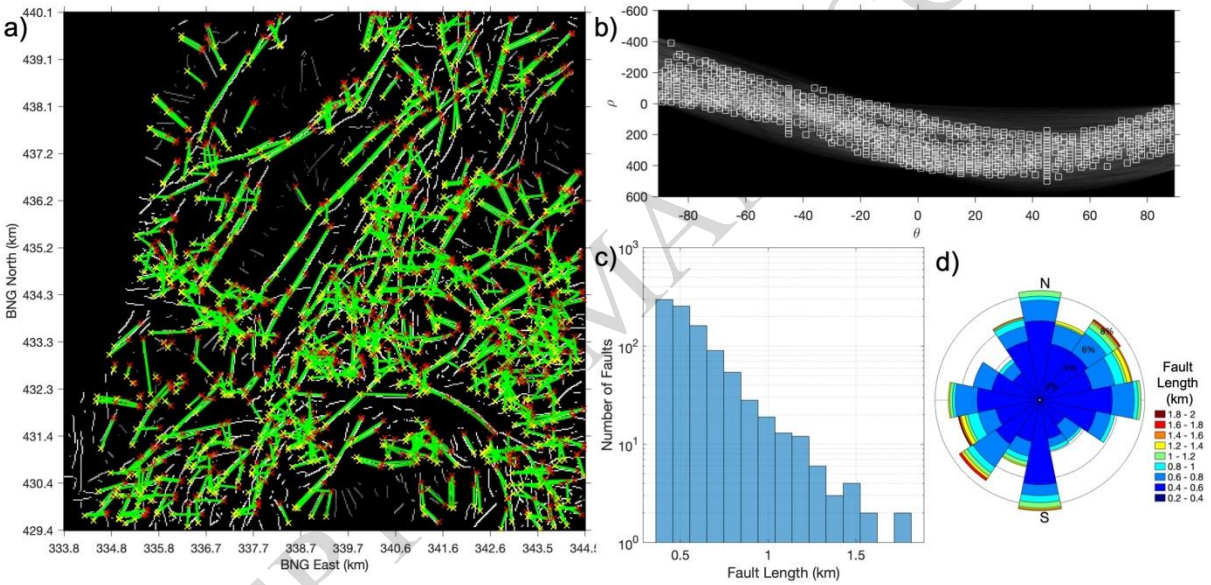

Figure 11

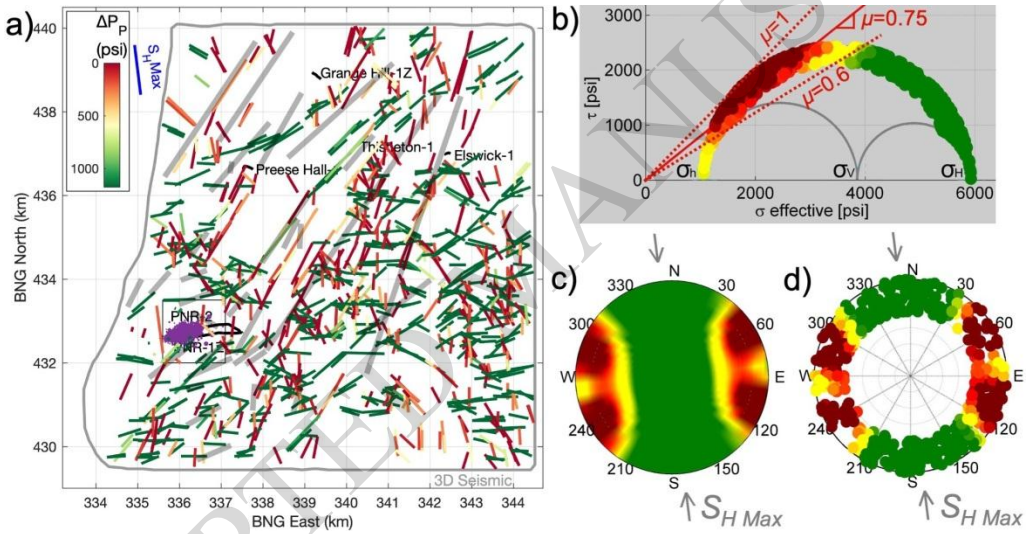

Table 1. Modelled fault rupture sizes as a function of earthquake magnitude. We assume a stress drop of 1 MPa, a fault aspect ratio of 1 (i.e., square), and a fault offset/fault length ratio of 1 %.

Magnitude	Fault Area [km^2]	Fault Length [km]	Fault Offset [m]
0	1×10^{-4}	0.01	0.1
1	1×10^{-3}	0.03	0.3
2	1×10^{-2}	0.1	1
3	0.1	0.3	3
4	1.0	1	10
5	10	3	34
6	100	10	107